Electronic structures and stability investigation of large band gap topological insulators MTl$_4$Te$_3$ (M = Cd, Hg)

Ying Li and Gang Xu*
Wuhan National High Magnetic Field Center & School of Physics, Huazhong University of Science and Technology, Wuhan 430074, China

(Received 30 May 2022; accepted 27 September 2022; published 10 October 2022)

By means of a ternary chemical potential phase diagram and phonon spectrum calculations, we propose that MTl$_4$Te$_3$ (M = Cd, Hg), which are derivatives of Tl$_5$Te$_3$, are thermodynamically and dynamically stable in the body-centered tetragonal crystal structure with $I4/mcm$ symmetry. Our electronic structure calculations confirm that a robust s-p band inversion occurs near the Fermi level in MTl$_4$Te$_3$, and a topological band gap of ~0.13 eV in CdTl$_4$Te$_3$ is induced by the spin-orbit coupling. These results suggest that MTl$_4$Te$_3$ are large band gap three-dimensional strong topological insulators that are stable and synthesizable in experiment and could be used to design efficient spin torque equipment and spin devices.

DOI: 10.1103/PhysRevMaterials.6.104201

I. INTRODUCTION

In the past two decades, topological electronic materials, including topological insulators (TIs) [1–5], topological semimetals [6–14], and topological superconductors (SCs) [5,15–20], have attracted great interest and reshaped perception of the materials. In particular, large band gap three-dimensional (3D) TIs have many intriguing properties in both fundamental physics [21–23] and device applications [24–28]. TIs with the spin momentum locked surface states are robust against perturbations and thus have high performance in spin torque [29,30], topotronic [31,32], and spintronic devices [33,34]. Furthermore, many exotic topological states are realized by modulating the TIs. For example, the quantum anomalous Hall (QAH) effect has been achieved by the magnetic doping in Bi$_2$Te$_3$ films [35–42]. Besides, topological superconductivity is reported in Cu-intercalated Bi$_2$Se$_3$ (Cu$_x$Bi$_2$Se$_3$) [17,18,43,44], Bi$_2$Te$_3$ under high pressure [45], and TI/SC heterostructures [46]. However, easily synthesized TIs with a relatively large band gap and clear two-dimensional (2D) Dirac-cone surface states such as the Bi$_2$Se$_3$ family [33,34,40,47–49] have remained rare until now. Therefore it is desirable to search for large band gap 3D TIs for potential utilizations.

First-principles calculations have played remarkable roles in the development of topological physics and topological materials. Many topological materials are predicted by first-principles calculations firstly, and then confirmed by experiments, including the HgTe quantum well [2,50], the bismuth antimony alloy Bi$_{1-x}$Sb$_x$ [22,51,52], the Bi$_2$Se$_3$ family of TIs [33,34,40,47–49], the topological crystalline insulator (TCI) SnTe [13,14], topological semimetals [6,7,11,12,53–59], and so on. Recently, Tl$_5$Te$_3$ [60] has been found to be a topological material that hosts Dirac surface states at 0.5 eV above the Fermi level (E_F). Since then, by using 4c site substitution, many derivatives MTl$_4$Te$_3$ (M = Cu, Sn, Mo, Pb, Bi, Sb, La, Nd, Sm, Gd, Tb, Dy, Er, Tm) [61–65] have been experimentally synthesized and reported. Among them, SnTl$_4$Te$_3$ with an eight-electron configuration was expected to be a TI. Unfortunately, the band inversion in SnTl$_4$Te$_3$ disappears, so that it becomes a trivial insulator [66,67].

Inspired by the above understanding, we propose that CdTl$_4$Te$_3$ and HgTl$_4$Te$_3$ are large band gap 3D strong topological insulators that are stable and synthesizable experimentally, through the 4c site substitution of Cd or Hg. For this purpose, a ternary chemical potential phase diagram with precursors and a convex hull diagram are constructed. Both of them demonstrate that CdTl$_4$Te$_3$ is thermodynamically stable and easily synthesized under Cd-rich, Tl$_2$Te$_3$-rich, and Tl-poor conditions. The phonon spectrum reveals that CdTl$_4$Te$_3$ adopts the body-centered tetragonal structure with $I4/mcm$ symmetry. Further electronic structure calculations identify that a robust band inversion between Cd-5s and Te-5p orbitals exists at the Γ point even without spin-orbit coupling (SOC). When SOC is considered, a topological band gap of ~0.13 eV is induced in CdTl$_4$Te$_3$, which is larger than the energy scale at room temperature in theory. As a result, one single Dirac cone formed by the topological surface states is discovered at the $\bar{\Gamma}$ point of the surface. The corresponding left-hand momentum locking texture is also studied, which can be applied in the design of efficient spin torque equipment and spin devices. Finally, the topological electronic structures and stability of the other derivative, HgTl$_4$Te$_3$, are discussed, which is expected to possess the same crystal structure and strong-TI nature as CdTl$_4$Te$_3$.

II. CRYSTAL STRUCTURES AND METHODOLOGY

In this paper, the same crystal structure as that of SnTl$_4$Te$_3$, i.e., the body-centered tetragonal phase with $I4/mcm$ space group (No. 140, D_{4h}^{18}) as shown in Fig. 1(a), is used for

*gangxu@hust.edu.cn

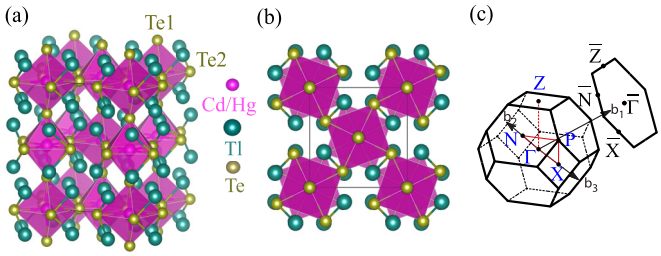

FIG. 1. (a) The unit cell of $CdTl_4Te_3$. (b) Top view of the unit cell. (c) Bulk BZ and its projection to the (100) surface of its primitive cell. The high-symmetry k path is indicated.

the calculation of MTl_4Te_3 (M = Cd, Hg). The corresponding first Brillouin zone (BZ) [68] and its projection on the (100) surface of the primitive cell are displayed in Fig. 1(c). In Fig. 1(a), the M atom locates at Wyckoff position 4c (0.5, 0.5, 0.0) which is the center of the corner-sharing $CdTe_6$ octahedron, Tl is located at 16l (x_1, $0.5 + x_1$, z_1), and two types of Te locate at 4a (0.5, 0.5, 0.25) and 8h ($-x_2$, $-x_2 + 0.5$, 0.0). The lattice parameters and atomic coordinates x_1, x_2, and z_1 are fully relaxed. The detailed structure information of MTl_4Te_3 is summarized in Table I. Besides, all the compounds used in our ternary phase diagram calculation are based on their ground phase in experiment, and their crystal parameters are fully relaxed as tabulated in Table I to make the energies comparable.

Our first-principles calculations are performed using the Vienna *ab initio* simulation package [69,70] with the projector augmented wave method [71]. The energy cutoff is set as 400 eV, and $9 \times 9 \times 7$ k meshes are adopted. The local-density approximation (LDA) type of exchange-correlation potential [72] is used in all calculations. All the different compositions $Cd_lTl_mTe_n$ are fully relaxed until the Hellmann-Feynman forces on each atom are less than 0.01 eV/Å and the total energy converges up to 10^{-6} eV. The ternary phase diagram is constructed by calculating the total energy of $Cd_lTl_mTe_n$ without SOC. The phonon spectrum calculations are carried out using the PHONOPY code [73] with a $2 \times 2 \times 2$ supercell through the density functional perturbation theory approach [74]. The band inversion is further confirmed by the modified Becke-Johnson (MBJ) potential [75] with the MBJ parameter C_{MBJ} set as 1.35. We note that $C_{\mathrm{MBJ}} \approx 1.1$–1.7 is usually used for semiconductors including IIB-VIA compounds as proposed by Tran, Blaha, and co-workers [75,76]. Its reliability and accuracy have been identified to be at the same level as the hybrid functional [77] and GW methods [78] for a wide variety of semiconductors [76,79–85]. The maximally localized Wannier functions are constructed using the

TABLE I. Detailed crystallographic information of corresponding compounds used in Fig. 2.

Compound	Space group	a, b, c (Å)	Fractional atomic coordinates
Cd	$P6_3/mmc$	$a = 2.9179$	Cd 2c $\left(\frac{1}{3}\ \frac{2}{3}\ 0.25\right)$
		$c = 5.3842$	
Tl	$P6_3/mmc$	$a = 3.4108$	Tl 2c $\left(\frac{1}{3}\ \frac{2}{3}\ 0.25\right)$
		$c = 5.4269$	
Te	$P3_121$	$a = 4.2786$	Te 3a $\left(0.2879\ 0\ \frac{1}{3}\right)$
		$c = 5.9249$	
CdTe	F-43m	$a = 6.4082$	Cd 4a (0.0 0.0 0)
			Te 4c (0.25 0.25 0.25)
TlTe	$I4/mcm$	$a = 12.6445$	Tl 16k (0.0783 0.2300 0.0)
		$c = 6.0775$	Te1 8h (0.1663 0.6663 0.25)
			Te2 4d (0.0 0.5 0.0)
			Te3 4a (0.0 0.0 0.25)
Tl_2Te_3	$C2/c$	$a = 12.8449$	Tl1 8f (0.8947 0.6452 0.5521)
	$\alpha = \gamma = 90°$	$b = 6.3989$	Te1 8f (0.6817 0.6379 0.0860)
	$\beta = 144.9264°$	$c = 13.0071$	Te2 4e (0.0 0.8703 0.25)
$CdTlTe_2$	P-3m1	$a = 4.2425$	Cd 1a (0.0 0.0 0.0)
		$c = 7.3925$	Tl 1b (0.0 0.0 0.5)
			Te 2d $(\frac{1}{3}\ \frac{2}{3}\ 0.2236)$
Tl_5Te_3	$I4/mcm$	$a = 8.6689$	Tl1 4c (0.5 0.5 0.0)
		$c = 12.6155$	Tl2 16l (0.1476 0.6476 0.1607)
			Te1 4a (0.5 0.5 0.25)
			Te2 8h (0.6565 0.1565 0.0)
$CdTl_4Te_3$	$I4/mcm$	$a = 8.5120$	Cd 4c (0.5 0.5 0.0)
		$c = 12.2642$	Tl 16l (0.1452 0.6452 0.1651)
			Te1 4a (0.5 0.5 0.25)
			Te2 8h (0.6624 0.1624 0.0)
$HgTl_4Te_3$	$I4/mcm$	$a = 8.6668$	Hg 4c (0.5 0.5 0.0)
		$c = 12.1854$	Tl 16l (0.1460 0.6460 0.1624)
			Te1 4a (0.5 0.5 0.25)
			Te2 8h (0.6599 0.1599 0.0)

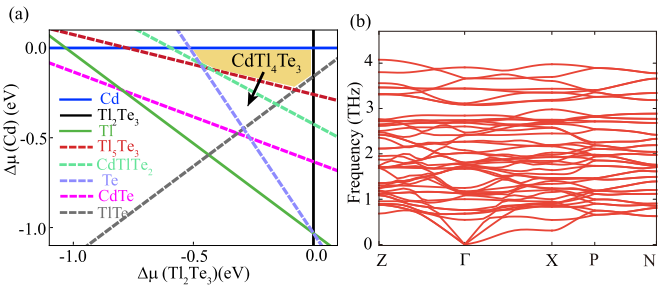

FIG. 2. (a) The ternary phase diagram of $CdTl_4Te_3$ with respect to the chemical potentials of Cd, Tl_2Te_3, and Tl, $\Delta\mu(\mathrm{Tl}) = \frac{1}{2}[E^F(\mathrm{CTT}) - \Delta\mu(\mathrm{Tl_2Te_3}) - \Delta\mu(\mathrm{Cd})]$. (b) The phonon dispersion curves of $CdTl_4Te_3$ without SOC.

WANNIER90 package [86] based on the MBJ+SOC calculations. The surface states are calculated by the iterative Green's function method as implemented in the WANNIERTOOLS package [87].

III. THE STABILITY OF $CdTl_4Te_3$

In this section, we would like to take $CdTl_4Te_3$ as an example to study its thermodynamical and dynamical stability. By choosing three stable compounds with Cd, Tl, and Tl_2Te_3 as the precursor materials, the target compound $CdTl_4Te_3$ can be synthesized by the following reaction:

$$\mathrm{Tl_2Te_3} + \mathrm{Cd} + 2\mathrm{Tl} \rightarrow \mathrm{CdTl_4Te_3}. \tag{1}$$

A phase diagram as a function of the precursors' chemical potentials could determine the ranges of the experimental synthesis conditions within which the target compound can be stabilized and within which the undesired competing phases are formed by varying the composition of precursors [88–93]. In general, the synthesis process can be understood as the exchange of elemental components between precursors and the forming phases. Therefore the formation energies of all forming compounds $\mathrm{Cd}_l\mathrm{Tl}_m\mathrm{Te}_n$ could be expressed as

$$E^F(\mathrm{Cd}_l\mathrm{Tl}_m\mathrm{Te}_n) = l\Delta\mu(\mathrm{Cd}) + \frac{n}{3}\Delta\mu(\mathrm{Tl_2Te_3}) + \left(m - \frac{2n}{3}\right)\Delta\mu(\mathrm{Tl}), \tag{2}$$

where $\Delta\mu(i) = \mu(i) - E^T(i)$, with i = Cd, Tl, and Tl_2Te_3, are the chemical potentials of the precursors referenced to the total energy of their ground states. Therefore Eq. (2) makes a connection between $\Delta\mu(i)$ and the experimental conditions, which means that the conditions should be rich in the corresponding precursor if $\Delta\mu(i)$ is close to zero and poor in that precursor if $\Delta\mu(i)$ has a large negative value. Based on our calculation, the formation energy of $CdTl_4Te_3$ is -1.032 eV/formula with respect to the precursors, which leads to two requirements for the chemical potentials. One is that each $\Delta\mu(i)$ could only vary between 0 and -1.032 eV. The other is that there are only two independent-variable chemical potentials. Therefore the phase diagram can be visualized by a 2D graph with variables $\Delta\mu(\mathrm{Tl_2Te_3})$ and $\Delta\mu(\mathrm{Cd})$ as shown in Fig. 2(a).

TABLE II. The calculated energy per formula used in Fig. 2.

Compound	E^T (eV)	E^F (eV)	$\widetilde{E}^F$ (eV)
Cd	−1.5037		
Tl	−2.9543		
Te	−3.8046	0.2237	
Tl_2Te_3	−17.9934		−0.6709
CdTe	−6.0324	−0.5004	−0.7241
TlTe	−7.1281	−0.1455	−0.3691
Tl_5Te_3	−28.0154	−1.1591	−1.8300
$CdTlTe_2$	−12.8369	−0.3224	−0.7697
$CdTl_4Te_3$	−26.4372	−1.0315	−1.7025

The competing phases, such as $CdTlTe_2$, TlTe, Tl_5Te_3, CdTe, and Te, are considered. Their formation energies $E^F(\mathrm{Cd}_l\mathrm{Tl}_m\mathrm{Te}_n)$ with respect to the precursors are calculated and listed in Table II. Then the phase diagram of $CdTl_4Te_3$ as a function of the chemical potentials $\Delta\mu(\mathrm{Cd})$, $\Delta\mu(\mathrm{Tl_2Te_3})$, and $\Delta\mu(\mathrm{Tl})$ is constructed in Fig. 2(a) by using a general scheme [89,90,93]. More details are described in the Supplemental Material (SM) [94]. Yielding to the constraint $\Delta\mu(i) \approx 0$ to -1.032 eV, the whole allowed chemical potential region is restricted in the triangle surrounded by $\Delta\mu(\mathrm{Cd}) = 0$ (blue solid line), $\Delta\mu(\mathrm{Tl}) = 0$ (green solid line) and $\Delta\mu(\mathrm{Tl_2Te_3}) = 0$ (black solid line). Our results reveal that $CdTl_4Te_3$ is most stable against other competing compounds in the orange region manifested by the phase separation lines $\Delta\mu(\mathrm{Tl_5Te_3}) = 0$, $\Delta\mu(\mathrm{CdTlTe_2}) = 0$, $\Delta\mu(\mathrm{TlTe}) = 0$, and $\Delta\mu(\mathrm{Te}) = 0$. Here, $\Delta\mu(\mathrm{Cd}_l\mathrm{Tl}_m\mathrm{Te}_n) = \mu(\mathrm{Cd}_l\mathrm{Tl}_m\mathrm{Te}_n) - E^F(\mathrm{Cd}_l\mathrm{Tl}_m\mathrm{Te}_n)$ is the chemical potential of a competing phase that is a function of the precursor's chemical potentials. The competing phase $\mathrm{Cd}_l\mathrm{Tl}_m\mathrm{Te}_n$ will precipitate out at $\Delta\mu(\mathrm{Cd}_l\mathrm{Tl}_m\mathrm{Te}_n) = 0$ and become unstable with a negative value. These results clearly demonstrate that $CdTl_4Te_3$ is easy to synthesize under Cd-rich, Tl_2Te_3-rich, and Tl-poor conditions. We would like to recall that the abundance of precursors is relative yielding to $E^F(\mathrm{CdTl_4Te_3}) = -1.032$ eV and Eq. (2). By increasing $\Delta\mu(\mathrm{Tl})$ along the black arrow in Fig. 2(a), it means that Tl grows more and more rich while Cd and Tl_2Te_3 become poor. When the arrow crosses the $\Delta\mu(\mathrm{Tl_5Te_3}) = 0$ and $\Delta\mu(\mathrm{CdTlTe_2}) = 0$ lines, $CdTl_4Te_3$ becomes unstable accompanied with the precipitation of Tl_5Te_3 and $CdTlTe_2$, and the following decomposition will take place:

$$\begin{aligned} \mathrm{CdTl_4Te_3} &\rightarrow \mathrm{Tl_5Te_3} + 3\mathrm{TlTe} + 2\mathrm{Cd}, \\ \mathrm{CdTl_4Te_3} &\rightarrow \mathrm{CdTlTe_2} + \mathrm{TlTe} + 2\mathrm{Tl}. \end{aligned} \tag{3}$$

According to our calculations, the energy of the products on the right is 0.234 and 0.564 eV higher than the energy on the left, respectively.

Convex hull analysis is another useful method to investigate the thermodynamical stability [95,96]. In this way, the formation energy of all possible atomic configurations with respect to constituent elements needs to be calculated, which is defined as $\widetilde{E}^F = E^T(\mathrm{Cd}_l\mathrm{Tl}_m\mathrm{Te}_n) - lE^T(\mathrm{Cd}) - mE^T(\mathrm{Tl}) - nE^T(\mathrm{Te})$. Using this definition, our calculations demonstrate that $CdTl_4Te_3$ is thermodynamically stable

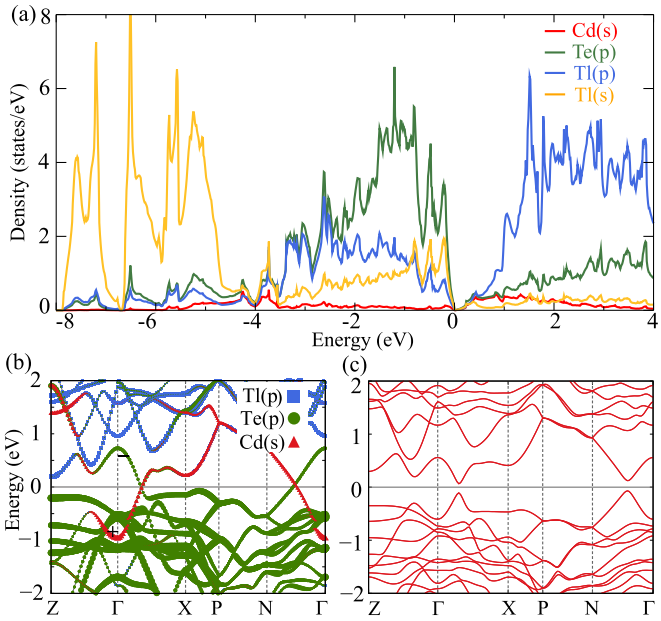

FIG. 3. The electronic properties of $CdTl_4Te_3$. (a) The projected DOS without SOC. (b) The band structure with spectral weight of Cd-5s (red), Te-5p (green), and Tl-6p (blue) orbitals without SOC. (c) The band structure with the MBJ potential including SOC.

against elements with formation energy of -0.213 eV/atom. With all possible $\widetilde{E}^F$ as listed in Table II, the convex hull diagram is constructed in Fig. S1 [94], which shows that only the binary compounds are on the convex hull, and all ternary compounds such as $CdTl_4Te_3$ and $CdTlTe_2$ are within a viable energy window for potentially metastable phases. Even so, we estimate that $CdTl_4Te_3$ is potentially synthesizable based on the following facts. One is that $CdTl_4Te_3$ is just a little above the convex hull with small energy and even 0.020 eV/atom lower than $CdTlTe_2$. Since $CdTlTe_2$ was already synthesized in 1969 [97], it is expected that it is highly feasible to synthesize $CdTl_4Te_3$ under proper conditions, especially under the Cd-rich, Tl_2Te_3-rich, and Tl-poor conditions in reaction equation (2).

To further check the dynamical stability of $CdTl_4Te_3$, the phonon spectrum based on the body-centered tetragonal phase with $I4/mcm$ symmetry is calculated. As shown in Fig. 2(b), there is no phonon mode with negative frequency in the entire BZ, which indicates that $CdTl_4Te_3$ is dynamically stable by adopting the body-centered tetragonal structure. The above thermodynamical and dynamical investigations strongly demonstrate that $CdTl_4Te_3$ is readily synthesized in experiment.

IV. ELECTRONIC PROPERTIES OF $CdTl_4Te_3$

The projected density of states (PDOS) of tetragonal $CdTl_4Te_3$ is calculated and plotted. As shown in Fig. 3(a), Tl-6s orbitals mainly contribute to the states between approximately -8 and -3.5 eV, while Tl-6p orbitals mainly contribute to the states above 0.3 eV. Considering the electronic configuration $6s^26p^1$ of Tl, we conclude that Tl favors the $+1$ valence in $CdTl_4Te_3$, similar to the valence of Tl atoms at the 16l site in Tl_5Te_3 [63,67]. The states in the energy range between approximately -3.5 and 0 eV are approximately from Te-5p orbitals with admixing of Tl-6p and Cd-5s states, which implies that the bonding between Cd, Tl, and Te does not consist of pure ionic bonds but has sizable metal-metal bond character. Figure 3(a) shows that the Cd-5s orbitals are almost empty and mainly contribute the states between approximately 0 and 3 eV. Therefore we can understand the electron transfer roughly as follows. Each Tl atom donates one 6p electron, and each Cd atom donates two 5s electrons to the Te-5p orbitals. As a result, $CdTl_4Te_3$ is close to the electronic configuration of an atomic insulator with the fully filled subshell of Te^{2-}, Tl^{1+}, and Cd^{2+} ions approximately.

However, we notice that the Cd-5s orbitals are very extended, which also exhibits considerable amplitude under the E_F, implying a band inversion between the Cd-5s and Te-5p states. The character is further verified by the projected band structures in Fig. 3(b), which clearly demonstrates that the Cd-5s states with even parity are lower by 1.82 eV than Te-5p states with odd parity at the Γ point. The band inversion in $CdTl_4Te_3$ already occurs even without SOC and can be alternatively viewed as a consequence of the inert pair effect in chemistry, which is the propensity for the two electrons in the outermost 5s orbital to remain un-ionized in heavier elements [98], just like that in HgTe [1,2]. In Fig. 3(b), when SOC is excluded, the band crossing points between the Cd-5s and Te-5p states can be protected by time-reversal symmetry ($\mathcal{TRS}$) and inversion symmetry ($\mathcal{I}$) and form nodal rings as plotted in Fig. S2(a) [94]. Since LDA-type exchange-correlation potential usually overestimates band inversion between valence and conduction bands, the MBJ potential [75] is employed. The amplitude of band inversion in the LDA is reduced to 1.10 eV with MBJ calculations as shown in Fig. S2(b) [94]. Therefore the band inversion in $CdTl_4Te_3$ is robust against the functional potentials, and the more accurate calculation of the LDA with the MBJ semilocal exchange functional potential is adopted to investigate the electronic and topological properties in the following.

When SOC is considered, the nodal rings are all gapped, inducing a 0.13-eV band gap as shown in Fig. 3(c), which is larger than the energy scale at room temperature theoretically. For insulators with $\mathcal{I}$, the topological invariant ν_0 based on the Fu-Kane formula [99] can be characterized by the parity products ξ_i of the half numbers of the occupied states at eight time-reversal-invariant momentum (TRIM) points (Kramers pairs have the same parities). As shown in Fig. 1(b), there are the following TRIM points in the first BZ: one Γ (0.0, 0.0, 0.0), one Z (0.5, 0.5, -0.5), two X (0.0, 0.0, 0.5), and four N (0.5, 0.0, 0.0). Therefore only ξ_Γ and ξ_Z could determine the topological property of the tetragonal $CdTl_4Te_3$, while the other TRIM points always give the trivial products. Our calculations indicate $\xi_\Gamma = -1$ and $\xi_Z = 1$ and give rise to $\nu_0 = 1$. These results are consistent with the band inversion analysis at the Γ point and confirm that $CdTl_4Te_3$ is a strong TI.

V. TOPOLOGICAL PROPERTIES OF $CdTl_4Te_3$

We construct the maximally localized Wannier functions of the Cd-5s, Te-5p, and Tl-6p states to investigate the topological features more explicitly. The Wilson loop method [100]

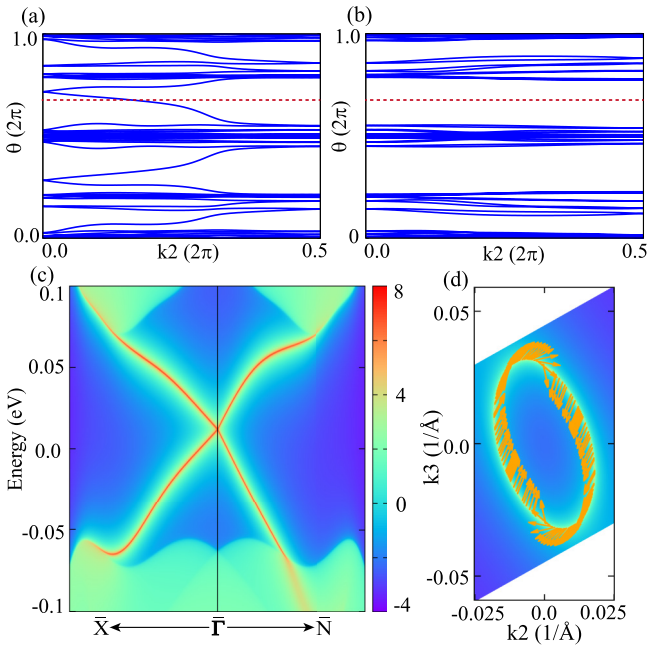

FIG. 4. The Wilson loops of (a) the k_2k_3 plane ($k_1 = 0$) and (b) the ($k_1 = \pi$) plane. (c) Band structures projected onto the (100) surface. (d) Topological surface states with chemical potential at 0.02 eV and corresponding spin texture on the (100) surface.

is used by calculating the evolution of Wannier charge centers for the occupied bands in the $k_1 = 0$ [Fig. 4(a)] and $k_1 = \pi$ planes [Fig. 4(b)]. The evolution lines cross the reference line (red dashed line) one time in Fig. 4(a), indicating that the $k_1 = 0$ plane corresponds to a quantum spin Hall system with a nontrivial 2D topological invariant. The evolution lines cross the reference line (red dashed line) zero times in Fig. 4(b), confirming that the $k_1 = \pi$ plane is a trivial 2D system. These results, combined with Wilson loops on other surface planes (Fig. S3) [94], give rise a complete topological index $\mathbb{Z}_2 = (1; 000)$, which further confirms that $CdTl_4Te_3$ falls into the strong-TI phase. In Fig. 4(c), we plot the surface electronic structures on the (100) surface by the iterative surface Green's function method [101,102]. Two robust surface states connect the valence and conduction bands and form a Dirac cone in the bulk gap at the $\bar{\Gamma}$ point due to the requirement of the $\mathcal{TRS}$. In Fig. 4(d), we plot the Fermi surfaces of the Dirac cone at 0.02 eV and their spin orientation, which exhibits a left-hand spin texture enclosing a π phase like that in Bi_2Se_3 [33], indicating a positive SOC in $CdTl_4Te_3$ [103]. Such kinds of spin momentum locking surface states have been reported that have very highly efficient performance in spin torque equipment [29,30] and spin devices [33,34].

VI. DISCUSSION AND CONCLUSION

Considering that Hg is isoelectronic with Cd in the IIB group of the periodic table, $HgTl_4Te_3$ is naturally expected to be stabilized into the same crystal structure of $CdTl_4Te_3$ with similar electronic structures and topological properties. By using the optimized structure parameters in Table I, the calculated formation energy of $HgTl_4Te_3$ through the reaction $Hg + 4Tl + 3Te \rightarrow HgTl_4Te_3$ is -1.459 eV with respect to elemental precursors. Limited by the stoichiometry, the products $\frac{1}{2}Tl_5Te_3 + HgTe + \frac{1}{2}TlTe + Tl$, $Tl_2Te_3 + Hg + 2Tl$, $3TlTe + Hg + Tl$, and $2TlTe + HgTe + 2Tl$ are taken into account by calculating the formation energies, which are equal to -1.397, -0.671, -1.107, and -1.035 eV, respectively. Obviously, $HgTl_4Te_3$ will be formed in the reaction because it is thermodynamically favorable. The MBJ-calculated band structures are presented in Fig. S4 [94]. As expected, the Hg-5s state with even parity is lower by 2.26 eV than the Te-5p state with odd parity at the Γ point. Furthermore, the 0.046-eV nontrivial band gap induced by SOC makes it a strong TI, which is similar to $CdTl_4Te_3$.

In conclusion, we predict that MTl_4Te_3 (M = Cd, Hg) are 3D topological insulators by using first-principles calculations. Our ternary chemical potential phase diagrams and phonon spectrum calculations demonstrate that MTl_4Te_3 (M = Cd, Hg) are both thermodynamically and dynamically stable in the body-centered tetragonal crystal structure with $I4/mcm$ symmetry. Further electronic structure calculations confirm that the nontrivial band topology stems from the band inversion between the M-5s and Te-5p orbitals at the Γ point, and the SOC-induced topological band gap is about 0.13 eV in $CdTl_4Te_3$, which is larger than the energy scale at room temperature in theory. The isolated-Dirac-cone-type surface states with left-hand helicity of the spin momentum locking texture are obtained in the (100) surface spectra at the $\bar{\Gamma}$ point. These results suggest that MTl_4Te_3 are synthesizable and suitable for use in the design of efficient spin torque equipment and spin devices, which should stimulate many experimental efforts in the future.

ACKNOWLEDGMENTS

This work was supported by the National Key Research and Development Program of China (Grant No. 2018YFA0307000) and the National Natural Science Foundation of China (Grant No. 11874022).

[1] X.-L. Qi, Y.-S. Wu, and S.-C. Zhang, Topological quantization of the spin Hall effect in two-dimensional paramagnetic semiconductors, Phys. Rev. B **74**, 085308 (2006).

[2] B. A. Bernevig, T. L. Hughes, and S.-C. Zhang, Quantum spin Hall effect and topological phase transition in HgTe quantum wells, Science **314**, 1757 (2006).

[3] A. P. Schnyder, S. Ryu, A. Furusaki, and A. W. W. Ludwig, Classification of topological insulators and superconductors in three spatial dimensions, Phys. Rev. B **78**, 195125 (2008).

[4] M. Z. Hasan and C. L. Kane, Topological insulators, Rev. Mod. Phys. **82**, 3045 (2010).

[5] X.-L. Qi and S.-C. Zhang, Topological insulators and superconductors, Rev. Mod. Phys. **83**, 1057 (2011).

[6] X. Wan, A. M. Turner, A. Vishwanath, and S. Y. Savrasov, Topological semimetal and Fermi-arc surface states in the

electronic structure of pyrochlore iridates, Phys. Rev. B **83**, 205101 (2011).

[7] G. Xu, H. Weng, Z. Wang, X. Dai, and Z. Fang, Chern Semimetal and the Quantized Anomalous Hall Effect in $HgCr_2Se_4$, Phys. Rev. Lett. **107**, 186806 (2011).

[8] A. A. Burkov and L. Balents, Weyl Semimetal in a Topological Insulator Multilayer, Phys. Rev. Lett. **107**, 127205 (2011).

[9] A. A. Zyuzin, S. Wu, and A. A. Burkov, Weyl semimetal with broken time reversal and inversion symmetries, Phys. Rev. B **85**, 165110 (2012).

[10] S. M. Young, S. Zaheer, J. C. Y. Teo, C. L. Kane, E. J. Mele, and A. M. Rappe, Dirac Semimetal in Three Dimensions, Phys. Rev. Lett. **108**, 140405 (2012).

[11] Z. Wang, Y. Sun, X.-Q. Chen, C. Franchini, G. Xu, H. Weng, X. Dai, and Z. Fang, Dirac semimetal and topological phase transitions in A_3Bi (A = Na, K, Rb), Phys. Rev. B **85**, 195320 (2012).

[12] Z. Wang, H. Weng, Q. Wu, X. Dai, and Z. Fang, Three-dimensional Dirac semimetal and quantum transport in Cd_3As_2, Phys. Rev. B **88**, 125427 (2013).

[13] T. H. Hsieh, H. Lin, J. Liu, W. Duan, A. Bansil, and L. Fu, Topological crystalline insulators in the SnTe material class, Nat. Commun. **3**, 982 (2012).

[14] S.-Y. Xu, C. Liu, N. Alidoust, M. Neupane, D. Qian, I. Belopolski, J. D. Denlinger, Y. J. Wang, H. Lin, L. A. Wray, G. Landolt, B. Slomski, J. H. Dil, A. Marcinkova, E. Morosan, Q. Gibson, R. Sankar, F. C. Chou, R. J. Cava, A. Bansil *et al.*, Observation of a topological crystalline insulator phase and topological phase transition in $Pb_{1-x}Sn_xTe$, Nat. Commun. **3**, 1192 (2012).

[15] L. Fu and C. L. Kane, Superconducting Proximity Effect and Majorana Fermions at the Surface of a Topological Insulator, Phys. Rev. Lett. **100**, 096407 (2008).

[16] X.-L. Qi, T. L. Hughes, S. Raghu, and S.-C. Zhang, Time-Reversal-Invariant Topological Superconductors and Superfluids in Two and Three Dimensions, Phys. Rev. Lett. **102**, 187001 (2009).

[17] Y. S. Hor, A. J. Williams, J. G. Checkelsky, P. Roushan, J. Seo, Q. Xu, H. W. Zandbergen, A. Yazdani, N. P. Ong, and R. J. Cava, Superconductivity in $Cu_xBi_2Se_3$ and its Implications for Pairing in the Undoped Topological Insulator, Phys. Rev. Lett. **104**, 057001 (2010).

[18] L. Fu and E. Berg, Odd-Parity Topological Superconductors: Theory and Application to $Cu_xBi_2Se_3$, Phys. Rev. Lett. **105**, 097001 (2010).

[19] G. Xu, B. Lian, P. Tang, X.-L. Qi, and S.-C. Zhang, Topological Superconductivity on the Surface of Fe-Based Superconductors, Phys. Rev. Lett. **117**, 047001 (2016).

[20] X.-L. Qi, T. L. Hughes, and S.-C. Zhang, Topological invariants for the Fermi surface of a time-reversal-invariant superconductor, Phys. Rev. B **81**, 134508 (2010).

[21] X.-L. Qi, T. L. Hughes, and S.-C. Zhang, Topological field theory of time-reversal invariant insulators, Phys. Rev. B **78**, 195424 (2008).

[22] D. Hsieh, Y. Xia, L. Wray, D. Qian, A. Pal, J. H. Dil, J. Osterwalder, F. Meier, G. Bihlmayer, C. L. Kane, Y. S. Hor, R. J. Cava, and M. Z. Hasan, Observation of unconventional quantum spin textures in topological insulators, Science **323**, 919 (2009).

[23] R. Li, J. Wang, X.-L. Qi, and S.-C. Zhang, Dynamical axion field in topological magnetic insulators, Nat. Phys. **6**, 284 (2010).

[24] G. Brumfiel, Topological insulators: Star material, Nature (London) **466**, 310 (2010).

[25] D. Pesin and A. H. MacDonald, Spintronics and pseudospintronics in graphene and topological insulators, Nat. Mater. **11**, 409 (2012).

[26] A. Politano, L. Viti, and M. S. Vitiello, Optoelectronic devices, plasmonics, and photonics with topological insulators, APL Mater. **5**, 035504 (2017).

[27] M. Ezawa, Topological Switch Between Second-Order Topological Insulators and Topological Crystalline Insulators, Phys. Rev. Lett. **121**, 116801 (2018).

[28] H. Wu, A. Chen, P. Zhang, H. He, J. Nance, C. Guo, J. Sasaki, T. Shirokura, P. N. Hai, B. Fang, S. A. Razavi, K. Wong, Y. Wen, Y. Ma, G. Yu, G. P. Carman, X. Han, X. Zhang, and K. L. Wang, Magnetic memory driven by topological insulators, Nat. Commun. **12**, 6251 (2021).

[29] A. R. Mellnik, J. S. Lee, A. Richardella, J. L. Grab, P. J. Mintun, M. H. Fischer, A. Vaezi, A. Manchon, E. A. Kim, N. Samarth, and D. C. Ralph, Spin-transfer torque generated by a topological insulator, Nature (London) **511**, 449 (2014).

[30] K. Kondou, R. Yoshimi, A. Tsukazaki, Y. Fukuma, J. Matsuno, K. S. Takahashi, M. Kawasaki, Y. Tokura, and Y. Otani, Fermi-level-dependent charge-to-spin current conversion by Dirac surface states of topological insulators, Nat. Phys. **12**, 1027 (2016).

[31] Q. Xu, Z. Song, S. Nie, H. Weng, Z. Fang, and X. Dai, Two-dimensional oxide topological insulator with iron-pnictide superconductor LiFeAs structure, Phys. Rev. B **92**, 205310 (2015).

[32] A. Q. Wang, X.-G. Ye, D.-P. Yu, and Z.-M. Liao, Topological semimetal nanostructures: From properties to topotronics, ACS Nano **14**, 3755 (2020).

[33] H. Zhang, C.-X. Liu, X.-L. Qi, X. Dai, Z. Fang, and S.-C. Zhang, Topological insulators in Bi_2Se_3, Bi_2Te_3 and Sb_2Te_3 with a single Dirac cone on the surface, Nat. Phys. **5**, 438 (2009).

[34] D. Hsieh, Y. Xia, D. Qian, L. Wray, J. Dil, F. Meier, J. Osterwalder, L. Patthey, J. Checkelsky, N. P. Ong, A. V. Fedorov, H. Lin, A. Bansil, D. Grauer, Y. S. Hor, R. J. Cava, and M. Z. Hasan, A tunable topological insulator in the spin helical Dirac transport regime, Nature (London) **460**, 1101 (2009).

[35] F. D. M. Haldane, Model for a Quantum Hall Effect Without Landau Levels: Condensed-Matter Realization of the "Parity Anomaly", Phys. Rev. Lett. **61**, 2015 (1988).

[36] M. Onoda and N. Nagaosa, Quantized Anomalous Hall Effect in Two-Dimensional Ferromagnets: Quantum Hall Effect in Metals, Phys. Rev. Lett. **90**, 206601 (2003).

[37] C.-X. Liu, X.-L. Qi, X. Dai, Z. Fang, and S.-C. Zhang, Quantum Anomalous Hall Effect in $Hg_{1-y}Mn_yTe$ Quantum Wells, Phys. Rev. Lett. **101**, 146802 (2008).

[38] H. Weng, R. Yu, X. Hu, X. Dai, and Z. Fang, Quantum anomalous Hall effect and related topological electronic states, Adv. Phys. **64**, 227 (2015).

[39] R. Yu, W. Zhang, H.-J. Zhang, S.-C. Zhang, X. Dai, and Z. Fang, Quantized anomalous Hall effect in magnetic topological insulators, Science **329**, 61 (2010).

[40] Y. Xia, D. Qian, D. Hsieh, L. Wray, A. Pal, H. Lin, A. Bansil, D. Grauer, Y. S. Hor, R. J. Cava, and M. Z. Hasan, Observation of a large-gap topological-insulator class with a single Dirac cone on the surface, Nat. Phys. **5**, 398 (2009).

[41] C.-Z. Chang, J. Zhang, X. Feng, J. Shen, Z. Zhang, M. Guo, K. Li, Y. Ou, P. Wei, L.-L. Wang, Z.-Q. Ji, Y. Feng, S. Ji, X. Chen, J. Jia, X. Dai, Z. Fang, S.-C. Zhang, K. He, Y. Wang *et al.*, Experimental observation of the quantum anomalous Hall effect in a magnetic topological insulator, Science **340**, 167 (2013).

[42] J. Ge, Y. Liu, J. Li, H. Li, T. Luo, Y. Wu, Y. Xu, and J. Wang, High-Chern-number and high-temperature quantum Hall effect without Landau levels, Natl. Sci. Rev. **7**, 1280 (2020).

[43] M. Kriener, K. Segawa, Z. Ren, S. Sasaki, and Y. Ando, Bulk Superconducting Phase with a Full Energy Gap in the Doped Topological Insulator $Cu_xBi_2Se_3$, Phys. Rev. Lett. **106**, 127004 (2011).

[44] L. A. Wray, S.-Y. Xu, Y. Xia, Y. S. Hor, D. Qian, A. V. Fedorov, H. Lin, A. Bansil, R. J. Cava, and M. Z. Hasan, Observation of topological order in a superconducting doped topological insulator, Nat. Phys. **6**, 855 (2010).

[45] J. L. Zhang, S. J. Zhang, H. M. Weng, W. Zhang, L. X. Yang, Q. Q. Liu, S. M. Feng, X. C. Wang, R. C. Yu, L. Z. Cao, L. Wang, W. G. Yang, H. Z. Liu, W. Y. Zhao, S. C. Zhang, X. Dai, Z. Fang, and C. Q. Jin, Pressure-induced superconductivity in topological parent compound Bi_2Te_3, Proc. Natl. Acad. Sci. USA **108**, 24 (2011).

[46] M.-X. Wang, C. Liu, J.-P. Xu, F. Yang, L. Miao, M.-Y. Yao, C. L. Gao, C. Shen, X. Ma, X. Chen, Z.-A. Xu, Y. Liu, S.-C. Zhang, D. Qian, J.-F. Jia, and Q.-K. Xue, The coexistence of superconductivity and topological order in the Bi_2Se_3 thin films, Science **336**, 52 (2012).

[47] Y. L. Chen, J. G. Analytis, J.-H. Chu, Z. K. Liu, S.-K. Mo, X. L. Qi, H. J. Zhang, D. H. Lu, X. Dai, Z. Fang, S. C. Zhang, I. R. Fisher, Z. Hussain, and Z.-X. Shen, Experimental realization of a three-dimensional topological insulator, Bi_2Te_3, Science **325**, 178 (2009).

[48] D. Hsieh, Y. Xia, D. Qian, L. Wray, F. Meier, J. H. Dil, J. Osterwalder, L. Patthey, A. V. Fedorov, H. Lin, A. Bansil, D. Grauer, Y. S. Hor, R. J. Cava, and M. Z. Hasan, Observation of Time-Reversal-Protected Single-Dirac-Cone Topological-Insulator States in Bi_2Te_3 and Sb_2Te_3, Phys. Rev. Lett. **103**, 146401 (2009).

[49] T. Arakane, T. Sato, S. Souma, K. Kosaka, K. Nakayama, M. Komatsu, T. Takahashi, Z. Ren, K. Segawa, and Y. Ando, Tunable Dirac cone in the topological insulator $Bi_{2-x}Sb_xTe_{3-y}Se_y$, Nat. Commun. **3**, 636 (2012).

[50] M. König, S. Wiedmann, C. Brüne, A. Roth, H. Buhmann, L. W. Molenkamp, X.-L. Qi, and S.-C. Zhang, Quantum spin Hall insulator state in HgTe quantum wells, Science **318**, 766 (2007).

[51] L. Fu and C. L. Kane, Topological insulators with inversion symmetry, Phys. Rev. B **76**, 045302 (2007).

[52] D. Hsieh, D. Qian, L. Wray, Y. Xia, Y. S. Hor, R. J. Cava, and M. Z. Hasan, A topological Dirac insulator in a quantum spin Hall phase, Nature (London) **452**, 970 (2008).

[53] Z. K. Liu, B. Zhou, Y. Zhang, Z. J. Wang, H. M. Weng, D. Prabhakaran, S.-K. Mo, Z. X. Shen, Z. Fang, X. Dai, Z. Hussain, and Y. L. Chen, Discovery of a three-dimensional topological Dirac semimetal, Na_3Bi, Science **343**, 864 (2014).

[54] S.-Y. Xu, C. Liu, S. K. Kushwaha, R. Sankar, J. W. Krizan, I. Belopolski, M. Neupane, G. Bian, N. Alidoust, T.-R. Chang, H.-T. Jeng, C.-Y. Huang, W.-F. Tsai, H. Lin, P. P. Shibayev, F.-C. Chou, R. J. Cava, and M. Z. Hasan, Observation of Fermi arc surface states in a topological metal, Science **347**, 294 (2015).

[55] H. Yi, Z. Wang, C. Chen, Y. Shi, Y. Feng, A. Liang, Z. Xie, S. He, J. He, Y. Peng, X. Liu, Y. Liu, L. Zhao, G. Liu, X. Dong, J. Zhang, M. Nakatake, M. Arita, K. Shimada, H. Namatame *et al.*, Evidence of topological surface state in three-dimensional Dirac semimetal Cd_3As_2, Sci. Rep. **4**, 6106 (2014).

[56] S. Jeon, B. B. Zhou, A. Gyenis, B. E. Feldman, I. Kimchi, A. C. Potter, Q. D. Gibson, R. J. Cava, A. Vishwanath, and A. Yazdani, Landau quantization and quasiparticle interference in the three-dimensional Dirac semimetal Cd_3As_2, Nat. Mater. **13**, 851 (2014).

[57] L. P. He, X. C. Hong, J. K. Dong, J. Pan, Z. Zhang, J. Zhang, and S. Y. Li, Quantum Transport Evidence for the Three-Dimensional Dirac Semimetal Phase in Cd_3As_2, Phys. Rev. Lett. **113**, 246402 (2014).

[58] H. Weng, C. Fang, Z. Fang, B. A. Bernevig, and X. Dai, Weyl Semimetal Phase in Noncentrosymmetric Transition-Metal Monophosphides, Phys. Rev. X **5**, 011029 (2015).

[59] X. Huang, L. Zhao, Y. Long, P. Wang, D. Chen, Z. Yang, H. Liang, M. Xue, H. Weng, Z. Fang, X. Dai, and G. Chen, Observation of the Chiral-Anomaly-Induced Negative Magnetoresistance in 3D Weyl Semimetal TaAs, Phys. Rev. X **5**, 031023 (2015).

[60] I. Schewe, P. Böttcher, and H. v. Schnering, The crystal structure of Tl_5Te_3 and its relationship to the Cr_5B_3 type, Z. Kristallogr. **188**, 287 (1989).

[61] S. Bradtmöller and P. Böttcher, Crystal structure of molybdenum tetrathallium tritelluride, $MoTl_4Te_3$, Z. Kristallogr. - Cryst. Mater. **209**, 75 (1994).

[62] S. Imamalieva, F. Sadygov, and M. Babanly, New thallium neodymium tellurides, Inorg. Mater. **44**, 935 (2008).

[63] S. Imamaliyeva, Tl_4GdTe_3 and Tl_4DyTe_3 - Novel structural Tl_5Te_3 analogues, Phys. Chem. Solid State **21**, 492 (2020).

[64] S. Z. Imamaliyeva, D. M. Babanly, D. B. Tagiev, and M. B. Babanly, Physicochemical aspects of development of multicomponent chalcogenide phases having the Tl_5Te_3 structure: A review, Russ. J. Inorg. Chem. **63**, 1704 (2018).

[65] S. Bradtmöller and P. Böttcher, Darstellung und Kristallstruktur von $SnTl_4Te_3$ und $PbTl_4Te_3$, Z. Anorg. Allg. Chem. **619**, 1155 (1993).

[66] K. E. Arpino, D. C. Wallace, Y. F. Nie, T. Birol, P. D. C. King, S. Chatterjee, M. Uchida, S. M. Koohpayeh, J.-J. Wen, K. Page, C. J. Fennie, K. M. Shen, and T. M. McQueen, Evidence for Topologically Protected Surface States and a Superconducting Phase in $[Tl_4](Tl_{1-x}Sn_x)Te_3$ Using Photoemission, Specific Heat, and Magnetization Measurements, and Density Functional Theory, Phys. Rev. Lett. **112**, 017002 (2014).

[67] K. E. Arpino, B. D. Wasser, and T. M. McQueen, Superconducting dome and crossover to an insulating state in $[Tl_4]Tl_{1-x}Sn_xTe_3$, APL Mater. **3**, 041507 (2015).

[68] W. Setyawan and S. Curtarolo, High-throughput electronic band structure calculations: Challenges and tools, Comput. Mater. Sci. **49**, 299 (2010).

[69] G. Kresse and J. Furthmüller, Efficiency of *ab-initio* total energy calculations for metals and semiconductors using a plane-wave basis set, Comput. Mater. Sci. **6**, 15 (1996).
[70] G. Kresse and J. Furthmüller, Efficient iterative schemes for *ab initio* total-energy calculations using a plane-wave basis set, Phys. Rev. B **54**, 11169 (1996).
[71] P. E. Blöchl, Projector augmented-wave method, Phys. Rev. B **50**, 17953 (1994).
[72] J. P. Perdew and A. Zunger, Self-interaction correction to density-functional approximations for many-electron systems, Phys. Rev. B **23**, 5048 (1981).
[73] A. Togo and I. Tanaka, First principles phonon calculations in materials science, Scr. Mater. **108**, 1 (2015).
[74] X. Gonze and C. Lee, Dynamical matrices, Born effective charges, dielectric permittivity tensors, and interatomic force constants from density-functional perturbation theory, Phys. Rev. B **55**, 10355 (1997).
[75] F. Tran and P. Blaha, Accurate Band Gaps of Semiconductors and Insulators with a Semilocal Exchange-Correlation Potential, Phys. Rev. Lett. **102**, 226401 (2009).
[76] D. Koller, F. Tran, and P. Blaha, Improving the modified Becke-Johnson exchange potential, Phys. Rev. B **85**, 155109 (2012).
[77] J. Heyd, G. E. Scuseria, and M. Ernzerhof, Hybrid functionals based on a screened Coulomb potential, J. Chem. Phys. **118**, 8207 (2003).
[78] L. Hedin, New Method for Calculating the One-Particle Green's Function with Application to the Electron-Gas Problem, Phys. Rev. **139**, A796 (1965).
[79] D. Koller, F. Tran, and P. Blaha, Merits and limits of the modified Becke-Johnson exchange potential, Phys. Rev. B **83**, 195134 (2011).
[80] D. J. Singh, Structure and optical properties of high light output halide scintillators, Phys. Rev. B **82**, 155145 (2010).
[81] Y.-S. Kim, M. Marsman, G. Kresse, F. Tran, and P. Blaha, Towards efficient band structure and effective mass calculations for III-V direct band-gap semiconductors, Phys. Rev. B **82**, 205212 (2010).
[82] D. J. Singh, Electronic structure calculations with the Tran-Blaha modified Becke-Johnson density functional, Phys. Rev. B **82**, 205102 (2010).
[83] S. Küfner, L. Matthes, and F. Bechstedt, Quantum spin Hall effect in $\alpha - \mathrm{Sn/CdTe}(001)$ quantum-well structures, Phys. Rev. B **93**, 045304 (2016).
[84] J. Lee, A. Seko, K. Shitara, K. Nakayama, and I. Tanaka, Prediction model of band gap for inorganic compounds by combination of density functional theory calculations and machine learning techniques, Phys. Rev. B **93**, 115104 (2016).
[85] T. Rauch, M. A. L. Marques, and S. Botti, Accurate electronic band gaps of two-dimensional materials from the local modified Becke-Johnson potential, Phys. Rev. B **101**, 245163 (2020).
[86] A. A. Mostofi, J. R. Yates, G. Pizzi, Y.-S. Lee, I. Souza, D. Vanderbilt, and N. Marzari, An updated version of wannier90: A tool for obtaining maximally-localised Wannier functions, Comput. Phys. Commun. **185**, 2309 (2014).
[87] Q. Wu, S. Zhang, H.-F. Song, M. Troyer, and A. A. Soluyanov, WannierTools: An open-source software package for novel topological materials, Comput. Phys. Commun. **224**, 405 (2018).
[88] J. M. Clary, A. M. Holder, and C. B. Musgrave, Computationally predicted high-throughput free-energy phase diagrams for the discovery of solid-state hydrogen storage reactions, ACS Appl. Mater. Interfaces **12**, 48553 (2020).
[89] A. P. Jaroenjittichai, Formation energies and chemical potential diagrams of II-Ge-N_2 semiconductors, Integr. Ferroelectr. **175**, 186 (2016).
[90] D. Mutter, D. F. Urban, and C. Elsässer, Determination of formation energies and phase diagrams of transition metal oxides with DFT$+U$, Materials **13**, 4303 (2020).
[91] H. Yokokawa, T. Kawada, and M. Dokiya, Construction of chemical potential diagrams for metal-metal-nonmetal systems: Applications to the decomposition of double oxides, J. Am. Ceram. Soc. **72**, 2104 (1989).
[92] H. Yokokawa, Generalized chemical potential diagram and its applications to chemical reactions at interfaces between dissimilar materials, J. Phase Equilib. **20**, 258 (1999).
[93] K. T. Jacob, T. H. Okabe, T. Uda, and Y. Waseda, System Cu-Rh-O: Phase diagram and thermodynamic properties of ternary oxides $CuRhO_2$ and $CuRh_2O_4$, Bull. Mater. Sci. **22**, 741 (1999).
[94] See Supplemental Material at http://link.aps.org/supplemental/10.1103/PhysRevMaterials.6.104201 later for details.
[95] A. Sharan and S. Lany, Computational discovery of stable and metastable ternary oxynitrides, J. Chem. Phys. **154**, 234706 (2021).
[96] Y. Sun, J. Lv, Y. Xie, H. Liu, and Y. Ma, Route to a Superconducting Phase above Room Temperature in Electron-Doped Hydride Compounds under High Pressure, Phys. Rev. Lett. **123**, 097001 (2019).
[97] G. Guseinov, G. Abdullayev, E. Kerimova, R. Gamidov, and G. Guseinov, Structural and physical properties of three-component $CdInS_2$ (Se_2, Te_2) compounds, Mater. Res. Bull. **4**, 807 (1969).
[98] P. Narang, C. A. C. Garcia, and C. Felser, The topology of electronic band structures, Nat. Mater. **20**, 293 (2021).
[99] L. Fu, C. L. Kane, and E. J. Mele, Topological Insulators in Three Dimensions, Phys. Rev. Lett. **98**, 106803 (2007).
[100] R. Yu, X. L. Qi, A. Bernevig, Z. Fang, and X. Dai, Equivalent expression of $\mathbb{Z}_2$ topological invariant for band insulators using the non-Abelian Berry connection, Phys. Rev. B **84**, 075119 (2011).
[101] M. P. L. Sancho, J. M. L. Sancho, and J. Rubio, Quick iterative scheme for the calculation of transfer matrices: Application to Mo (100), J. Phys. F: Met. Phys. **14**, 1205 (1984).
[102] M. P. L. Sancho, J. M. L. Sancho, J. M. L. Sancho, and J. Rubio, Highly convergent schemes for the calculation of bulk and surface Green functions, J. Phys. F: Met. Phys. **15**, 851 (1985).
[103] S. Nie, G. Xu, F. B. Prinz, and S.-c. Zhang, Topological semimetal in honeycomb lattice LnSI, Proc. Natl. Acad. Sci. USA **114**, 10596 (2017).